Icarus 355 (2021) 114168

Contents lists available at ScienceDirect

Icarus

journal homepage: www.elsevier.com/locate/icarus

Dynamic aperture factor analysis/target transformation (DAFA/TT) for Mg-serpentine and Mg-carbonate mapping on Mars with CRISM near-infrared data

Honglei Lin [a,b], J.D. Tarnas [c], J.F. Mustard [c], Xia Zhang [a,*], Yong Wei [b], Weixing Wan [b], F. Klein [d], J.R. Kellner [e]

[a] Aerospace Information Research Institute, Chinese Academy of Sciences, Beijing 100101, China
[b] Institute of Geology and Geophysics, Chinese Academy of Sciences, Beijing 100029, China
[c] Dept. of Earth, Environmental, and Planetary Sciences, Brown University, RI 02912, The United States of America
[d] Dept. of Marine Chemistry and Geochemistry, Woods Hole Oceanographic Institution, MA 02543, The United States of America
[e] Institute at Brown for Environment and Society, Brown University, RI 02912, The United States of America

ARTICLE INFO

Keywords:
Dynamic aperture
Factor analysis and target transformation
Serpentine
Carbonate
Mars

ABSTRACT

Serpentine and carbonate are products of serpentinization and carbonation processes on Earth, Mars, and other celestial bodies. Their presence implies that localized habitable environments may have existed on ancient Mars. Factor Analysis and Target Transformation (FATT) techniques have been applied to hyperspectral data from the Compact Reconnaissance Imaging Spectrometer for Mars (CRISM) to identify possible serpentine and Mg-carbonate-bearing outcrops. FATT techniques are capable of suggesting the presence of individual spectral signals in complex spectral mixtures. Applications of FATT techniques to CRISM data thus far only evaluate whether an entire analyzed image ($\approx 3 \times 10^5$ pixels) may contain spectral information consistent with a specific mineral of interest. The spatial distribution of spectral signal from the possible mineral is not determined, making it difficult to validate a reported detection and also to understand the geologic context of any purported detections. We developed a method called Dynamic Aperture Factor Analysis/Target Transformation (DAFA/TT) to highlight the locations in a CRISM observation (or any similar laboratory or remotely acquired data set) most likely to contain spectra of specific minerals of interest. DAFA/TT determines the locations of possible target mineral spectral signals within hyperspectral images by performing FATT in small moving windows with different geometries, and only accepting pixels with positive detections in all cluster geometries as possible detections. DAFA/TT was applied to a hyperspectral image of a serpentinite from Oman for validation testing in a simplified laboratory setting. The mineral distribution determined by DAFA/TT application to the laboratory hyperspectral image was consistent with Raman analysis of the serpentinite sample. DAFA/TT also successfully mapped the spatial distribution of Mg-serpentine and Mg-carbonate previously detected in CRISM data using band parameter mapping and extraction of ratioed spectra. We applied DAFA/TT to CRISM images in some olivine-rich regions of Mars to characterize the spatial distribution of Mg-serpentine and Mg-carbonate-bearing outcrops.

1. Introduction

The search for habitable environments is a fundamental goal of Mars exploration. Planetary habitability for life as we know it requires liquid water, temperatures between −20 °C (Clarke et al., 2013) and 122 °C (Takai et al., 2008), redox energy availability, and sufficient protection from high levels of radiation and oxidation. The existence of serpentine, formed via hydrothermal alteration of ultramafic rocks (Kelley et al., 2005; Sleep et al., 2004; Evans et al., 2013; Schulte et al., 2006; Amador et al., 2017), is considered an indicator of planetary habitability (e.g., Russell et al., 2010; Vance et al., 2016). Serpentinization is a process which involves a series of dissolution, precipitation, and redox reactions affecting olivine and pyroxene in contact with water (Evans et al., 2013; McCollom et al., 2016). Serpentinization occurs in a wide range of temperature conditions (Miller et al., 2017; Chavagnac et al., 2013; Mayhew et al., 2013; Kelley et al., 2005; Sleep et al., 2004; Allen and

* Corresponding author.
E-mail address: zhangxia@radi.ac.cn (X. Zhang).

https://doi.org/10.1016/j.icarus.2020.114168
Received 20 February 2020; Received in revised form 28 August 2020; Accepted 13 October 2020
Available online 17 October 2020

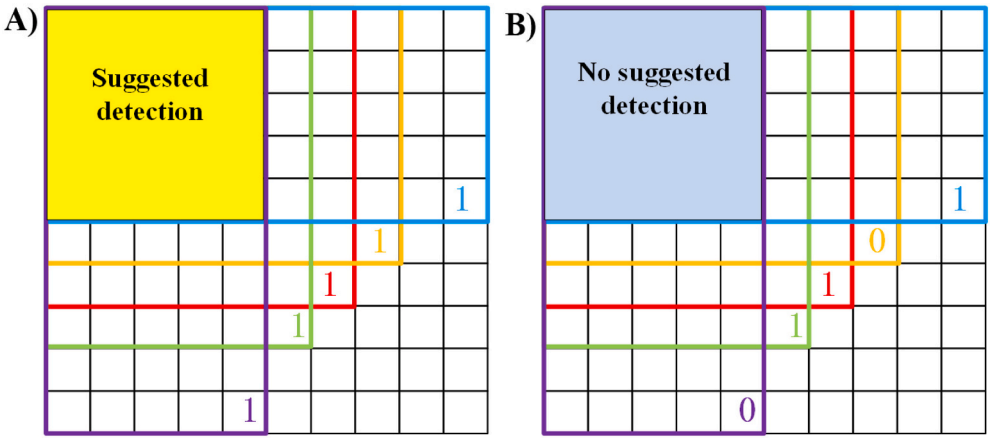

Fig. 1. An illustration of apertures used in DAFA/TT. A) FATT is applied to all pixel subsets (blue, orange, red, green, and purple) and if all the apertures return suggested detections (1), the pixels marked in yellow are considered as true suggested detections. B) If any apertures show negative suggestions (0), no suggested detection will be returned. The apertures are moved in single pixel increments. (For interpretation of the references to colour in this figure legend, the reader is referred to the web version of this article.)

Seyfried, 2003) and can sustain microbial ecosystems in terrestrial (e.g., Rempfert et al., 2017) and marine environments (e.g., Kelley et al., 2005; Schrenk et al., 2013) via generation of H_2—an electron donor—as a reaction product.

Under the right conditions, ultramafic rocks exposed to aqueous fluids enriched in dissolved inorganic carbon ($CO_{2(aq)}$) will form carbonate minerals at the expense of olivine, pyroxene, serpentine, brucite, magnetite, and talc (Klein and Garrido, 2011). The assemblage of serpentine and carbonate is therefore indicative of past water-rock alteration in the presence of CO_2 (e.g., Park et al., 2003) that likely generated H_2 through the oxidation of ferrous iron by water (e.g., McCollom et al., 2020). Carbonated serpentinites can also preserve biosignatures of subsurface chemolithotrophic microbial ecosystems over geological timescales (Klein et al., 2015). These lithologies would be feasibly detectable with instruments onboard NASA's Perseverance rover and China's Tianwen-1 rover.

Mg-rich serpentine exhibits characteristic absorptions in the 1.0–2.6 μm region, including absorption minima around 1.39 and 1.9 μm produced by OH^- and H_2O and a strong, asymmetric, narrow absorption centered around 2.325 μm Mg-OH combination band as well as a 2.50–2.51 μm symmetric absorption (Clark et al., 1990). The most diagnostic feature of Mg-rich serpentine is the relatively shallow absorption at ~2.12 μm, which is used to confidently identify this mineral in reflectance spectra (Amador et al., 2018). All serpentine discussed in this work is Mg-rich. Diagnostic absorptions in the 1.0–2.6 μm region consistent with carbonate minerals are paired absorption features centered near ~2.3 and ~ 2.5 μm that are overtones and combination tones of C—O stretching and bending fundamental vibrations (Hunt and Salisbury, 1971). These absorptions are centered at 2.34 and 2.54 for Ca-rich carbonate; 2.30 and 2.50 μm for Mg-rich carbonate; and 2.33 and 2.53 μm for Fe-rich carbonate (Hunt and Salisbury, 1971; Gaffey, 1987).

Visible-to-near infrared (VNIR) hyperspectral remote sensing observations permit characterization of the surface composition of Mars from meter to kilometer spatial scales. Such instruments include the Observatoire pour la Mineralogie, l'Eau, les Glaces et l'Activite (OMEGA) (Bibring et al., 2004) and the Compact Reconnaissance Imaging Spectrometer for Mars (CRISM) (Murchie et al., 2007). Both instruments revolutionized our understanding of aqueous mineralogy of Mars. Building on the discoveries of OMEGA, CRISM's higher spatial (18 m/pixel) and spectral resolution (6.55 nm/channel) expanded the number of detected mineral phases on Mars and better defined their geologic context. Carbonate-bearing outcrops on Mars have been identified in the Nili Fossae region using CRISM data (Bramble et al., 2017; Edwards and Ehlmann, 2016; Ehlmann et al., 2010; Ehlmann et al., 2009; Ehlmann et al., 2008; Goudge et al., 2017). Serpentine has been detected on the surface of Mars (e.g., Ehlmann et al., 2010), but recently Leask et al. (2018) showed that many of the spectral signals previously classified as serpentine detections likely result from a 2.1 μm artifact present in CRISM TRR3 I/F images that were processed using the custom filtering procedure as described in Seelos et al. (2011). Therefore, previous claimed detections of serpentine on Mars should be reevaluated.

Detection of minerals in hyperspectral images often begins with spectral parameter mapping (Pelkey et al., 2007; Viviano-Beck et al., 2014) to identify pixels where spectra exhibit features characteristic of specific minerals or mineral groups. Spectra extracted from these regions of interest are then compared with library spectra of well-characterized minerals to evaluate which minerals are present. Because diagnostic absorptions are commonly obscured by instrumental artifacts related to incomplete removal of atmospheric absorptions, instrument signal chain (e.g., the acquisition, amplification, transmission and processing of the signal), low signal-to-noise, as well as structured noise, researchers commonly minimize these effects by generating spectral ratios prior to visual interpretation (e.g., Mustard et al., 2008). Spectral ratios are created by ratioing the spectrum from a region of interest to a spectrum of a region showing unremarkable spectra (low spectral contrast), most optimally from the same detector columns as the target spectrum. This process removes common artifacts and noise features. However, it can sometimes introduce new artifacts and is time consuming (Carter et al., 2013; Thomas and Bandfield, 2017). Automatic/semi-automatic methods have been developed to improve methodological effectiveness and efficiency for detecting minerals on Mars in order to maximize the scientific return from the CRISM dataset (Thollot et al., 2012; Carter et al., 2013; Parente et al., 2014; Bultel et al., 2015; Thomas and Bandfield, 2017; Amador et al., 2018; Dundar et al., 2019).

Factor analysis (Malinowski, 1991) was originally applied to spectral datasets to characterize individual spectrally active chemical compounds introduced during chemical evolution via chromatography and titration (Schostack and Malinowski, 1993; Malinowski, 1996). In its first application to data from Mars, factor analysis and target transformation (FATT) was used to separate individually contributing surface and atmospheric spectral components in Thermal Emission Spectrometer (TES) data (Bandfield et al., 2000; Smith et al., 2000). It was later used to separate individual surface and atmospheric spectral components from spectra obtained by the Miniature Thermal Emission Spectrometer (Mini-TES) onboard NASA's Opportunity rover in Meridiani Planum (Glotch and Bandfield, 2006). FATT has been applied to CRISM VNIR data to identify images with possible phyllosilicate, carbonate, and sulfate minerals (Thomas and Bandfield, 2017). It has also been used to highlight CRISM images with possible serpentine and magnesite globally (Amador et al., 2018). Amador et al. (2018) surveyed all CRISM images between 70° N and 70° S with the FATT method to search for serpentine and Mg-carbonate. However, the only information returned by these FATT applications is whether the analyzed CRISM scene (≈100–400

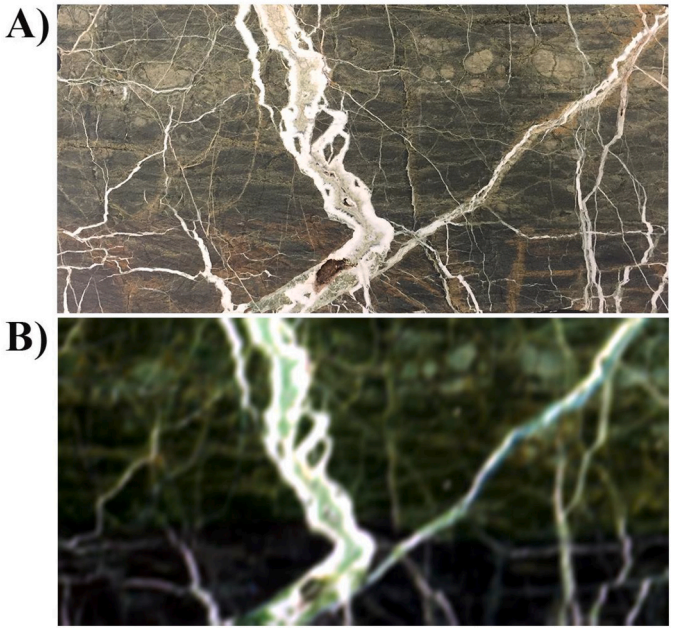

Fig. 2. The laboratory hyperspectral image data. A) Visible light picture of the cut rock surface of serpentinite (size: 10.5 cm × 19.5 cm) from the Oman ophiolite used in this analysis. B) RGB composite of the hyperspectral data measured with a Headwall imaging spectrometer (R: 2.14 μm, G: 1.75 μm, B: 1.20 μm). The white veins consist of calcium carbonate with traces of serpentine present. The green matrix primarily consists of serpentine with variable amounts of magnetite and minor red iron oxides. (For interpretation of the references to colour in this figure legend, the reader is referred to the web version of this article.)

km^2) may contain the specific mineral of interest. No information regarding the location of the mineral is generated, making it difficult to validate and assess the results in the context of previously applied mineral detection techniques. While these previous applications of FATT to CRISM data have claimed detection of many different phyllosilicates, carbonates, and sulfates in hundreds of CRISM images (Thomas and Bandfield, 2017; Amador et al., 2018), only a few I/F spectra were reported, e.g., kaolinite in FRT0000C202 by Thomas and Bandfield (2017), magnesite in HRL000095C7 by Amador et al. (2018), and saponite or talc in FRT0001756E by Amador et al. (2018). This lack of validation via I/F spectra extraction for hundreds of reported mineral detections leaves open the possibility of false positive results. Additionally, the artifact discovered by Leask et al. (2018) further calls into question possible serpentine detections reported in these studies, as well as all previous serpentine detections on Mars where a 2.1 μm feature in radiance data has not been reported.

Here we present a new application of factor analysis and target transformation, termed Dynamic Aperture Factor Analysis/Target Transformation (DAFA/TT), to suggest the distribution of serpentine and carbonate deposits on Mars. The technique is not limited to these two minerals, but they are the focus of this first analysis. Application of a dynamic aperture results in predicted locations for target minerals within CRISM images, allowing for extraction of supporting I/F spectra. DAFA/TT calculates eigenvectors and performs target transformation in differently shaped apertures that move across the image in single pixel increments. This generates suggested detections of minerals in complex convolutions with higher spatial precision than previous techniques. The method was applied to hyperspectral laboratory data of a well-characterized serpentinite sample as well as to previously analyzed CRISM images with reported serpentine and Mg-carbonate I/F spectra. We also applied this method to CRISM images in olivine-rich regions of Mars (Koeppen and Hamilton, 2008), mainly Ganges Chasma and parts of Nili Fossae (Table S1), to locate I/F spectra consistent with the presence of serpentine.

2. Methods

2.1. Factor analysis and target transformation

Factor analysis identifies independently varying spectral components in a mixed system, referred to as eigenvectors, given an input dataset of multiple spectral measurements (Malinowski, 1996; Bandfield et al., 2000; Smith et al., 2000; Glotch and Bandfield, 2006; Thomas and Bandfield, 2017; Amador et al., 2018). Calculated eigenvectors are signals contributing variance to the given spectral dataset and can contain spectral features of individual components within the measured mixture. Previous FATT applications to entire CRISM images considered the first 10 orthogonal eigenvectors of the covariance matrix to be the independently varying components comprising the signal subspace of these images (Thomas and Bandfield, 2017; Amador et al., 2018). Target transformation is the linear least squares fitting of combinations of factor-analysis-derived eigenvectors—assumed or determined to constitute the signal subspace—to library spectra of characterized materials. Theoretically, this can be used to reconstruct spectral endmembers, including minerals of interest that are present within a dataset of spectral mixtures (Bandfield et al., 2000; Smith et al., 2000; Glotch and Bandfield, 2006; Thomas and Bandfield, 2017; Amador et al., 2018). Library spectra that are fit during target transformation can be collected from standard spectral libraries (e.g., Reflectance Experiment Laboratory database, USGS spectral library) or from hyperspectral images. If the target transformation fit between a linear combination of eigenvectors and a library spectrum matches to an acceptable level, then the material associated with the library spectrum is likely a component present in the dataset.

FATT can provide spectral evidence for the presence of specific minerals on Mars that exist in complex convolutions (Amador et al., 2018; Thomas and Bandfield, 2017) or that possess weak spectral absorptions. FATT is best suited to detect hydrated phases with narrow spectral absorptions in CRISM data (Thomas and Bandfield, 2017). Applications of FATT to CRISM data thus far have several key limitations: 1) Determination of the number of eigenvectors to use for target transformation is subjective. For example, using the first 10 eigenvectors corresponding to 10 largest eigenvalues for target transformation is an arbitrary choice. Using the first 20 or 30 eigenvectors would obtain better target transformation fits, while using the first 5 eigenvectors would lead to worse target transformation fits (Thomas and Bandfield, 2017). In general, using more eigenvectors increases the likelihood of introducing structured and random noise, and can lead to false positive detections. 2) Robust assessment methods for the fits between library spectra and modeled spectra are needed. 3) In previous applications of FATT to CRISM data (e.g., Amador et al., 2018; Thomas and Bandfield, 2017), the only result returned is whether the target mineral is likely present within the entire analyzed image. No information regarding the possible spatial distribution of the target mineral is generated, making it difficult to validate results and understand the geologic setting and context of possible detections.

2.2. Determination of eigenvectors

The hyperspectral signal identification by minimum error (Hysime) algorithm (Bioucas-Dias and Nascimento, 2008) objectively determines the eigenvectors that comprise the signal subspace of a spectral dataset. The Hysime algorithm estimates the signal and noise correlation matrices, then determines which subset of eigenvalues best represents the signal subspace by minimizing the sum of the projection error power with the noise power. The noise error is an increasing function of subspace dimension and can be estimated with multiple regression. The noise can be estimated based on eqs. (1)–(3).

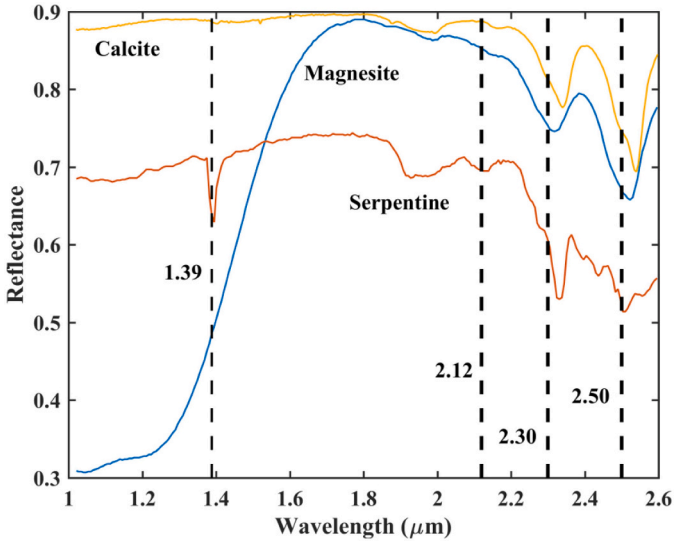

Fig. 3. Example spectra of serpentine (Serpentine 15 in Table S2), magnesite (Carbonate 48 in Table S2), and Ca-carbonate (CACB10) spectra provided by the RELAB database. Magnesite and Ca-carbonate show paired absorptions at ~2.3 and ~ 2.5 μm, serpentine exhibits absorptions at 1.39 μm, 2.33 μm, and 2.52 μm as well as a weak absorption at ~2.12 μm.

$$z_i = Z_{\alpha_i}\beta_i + \varepsilon_i \tag{1}$$

where, Z is the transpose of Y (Y is an L × N matrix where L is the number of bands and N is the number of pixels, which in this application constitutes spectra from the CRISM image), z_i is the ith column of Z, $Z_{\alpha i} = (z_1, \ldots, z_{i-1}, z_{i+1}, \ldots z_L)$ is the explanatory data matrix, β_i is the regression vector, and ε_i is the modeling error. The regression vector can be estimated using least squares:

$$\beta_{estimate\_i} = \left(Z_{\alpha_i}{}^T Z_{\alpha_i}\right)^{-1} Z_{\alpha_i}{}^T z_i \tag{2}$$

The noise can be estimated by:

$$\varepsilon_{estimate\_i} = z_i - Z_{\alpha_i}\beta_{estimate\_i} \tag{3}$$

The noise correlation matrix is:

$$R_n = \sum_i \varepsilon_{estimate\_i}\varepsilon_{estimate\_i}{}^T \Big/ N \tag{4}$$

The signal correlation matrix can be written as:

$$R_x = \sum_i (y_i - \varepsilon_{estimate\_i})(y_i - \varepsilon_{estimate\_i})^T \Big/ N \tag{5}$$

Then the eigenvectors of the signal correlation matrix R_x can be computed and are written as $E = (e_1, e_2, \ldots, e_L)$. The minimization function of the sum of projection error power and the noise power can be written as (Bioucas-Dias and Nascimento, 2008):

$$f = -diag\left(E^T R_y E\right) + 2diag\left(E^T R_n E\right) \tag{6}$$

$$R_y = \sum_i y_i y_i{}^T \Big/ N \tag{7}$$

The signal subspace dimension is the number of negative terms of f. The eigenvectors of R_x corresponding to these negative terms are the significant factors, comprising the signal subspace, that are used for target transformation.

2.3. Dynamic aperture factor analysis/target transformation

Dynamic Aperture Factor Analysis/Target Transformation (DAFA/TT) is a new application of FATT to hyperspectral image data. DAFA/TT analyzes hyperspectral data by defining an aperture and moving it incrementally across the entire image (Fig. 1). If a quantitatively good FATT fit to a library spectrum is found, that aperture location is saved, aggregating positive detections across the scene. By implementing multiple differently shaped apertures (e.g., of size 7 × 7 pixels, 5 × 10 pixels, 10 × 5 pixels etc.) and determining where positive detections from these different apertures overlap, we can locate high probability suggested detections for specific minerals of interest (or other spectrally active compounds). The DAFA/TT method, as applied in this specific study, determines the important eigenvectors within dynamic apertures (Fig. 1) via the Hysime algorithm.

Signal subspace eigenvectors determined using the Hysime algorithm are used for target transformation and compared to library spectra of serpentine and magnesite. The target transformation method used here is unconstrained linear least squares fitting (Keshava and Mustard, 2002). The library and modeled spectra are normalized (the I/F value of each wavelength divided by the sum of I/F in all wavelengths) to allow for root-mean-square error (RMSE) comparison between minerals with different reflectance scales, permitting robust assessment of fit quality. When the RMSE is less than a specified threshold, the aperture is considered to contain a positive suggested detection of the target mineral. There likely should be a slightly different threshold for each mineral due to the different shapes and depths of their absorption features, but at this stage optimization is sacrificed for automation. Pixels where possible detections from all apertures of differing geometries intersect are considered the best suggested locations for detections in that image (Fig. 1). Apertures are moved across the image in single pixel increments. Multiple shapes are used to remove edge detection pixels from individual apertures that do not contain the detected signal, trimming false-positive pixels from possible detections in apertures of each individual geometry. Clusters of suggested detections for minerals are produced, each of which has their own target-transformation-derived fit to an associated library spectrum. The selected RMSE fit threshold is used to generate these positive suggested detection clusters in an automated fashion. Modeled fits of each cluster are then inspected by a trained analyst who only approves fits containing diagnostic absorptions of the mineral of interest, removing the other suggested detection clusters and thus reducing false positives. Validation by a trained analyst is necessary because the critical factors for determining the resemblance of target transformation fits to real mineral spectra include the position, strength, and shape of diagnostic absorptions. Without an accepted mathematical metric for weighting these absorption features more heavily than other parts of the spectrum, we rely on visual inspection as our final step. Analyses of remotely acquired spectra from Mars and other planets commonly include a similar component of visual inspection (e.g., Ehlmann et al., 2009; Mustard et al., 2011).

3. Data collection

We analyzed laboratory imaging spectrometer data with DAFA/TT to test its functionality, and then applied it to map the distribution of magnesite and serpentine in CRISM scenes within some olivine-rich regions.

3.1. Laboratory data

3.1.1. Serpentinite sample

A serpentinite rock collected from the Oman ophiolite was chosen to test spatial accuracy of the DAFA/TT method. This hand sample contains variable amounts of serpentine, Ca-carbonate, magnetite, and red iron oxides. Its carbonate veins are distributed in various geometries and range in size from several millimeters to <1 mm (Fig. 2). Multiple generations of serpentinization are apparent in this rock, which contains a dark matrix of older magnetite-rich serpentine that is cross-cut by younger, light-green, and more magnetite-poor serpentine proximal to

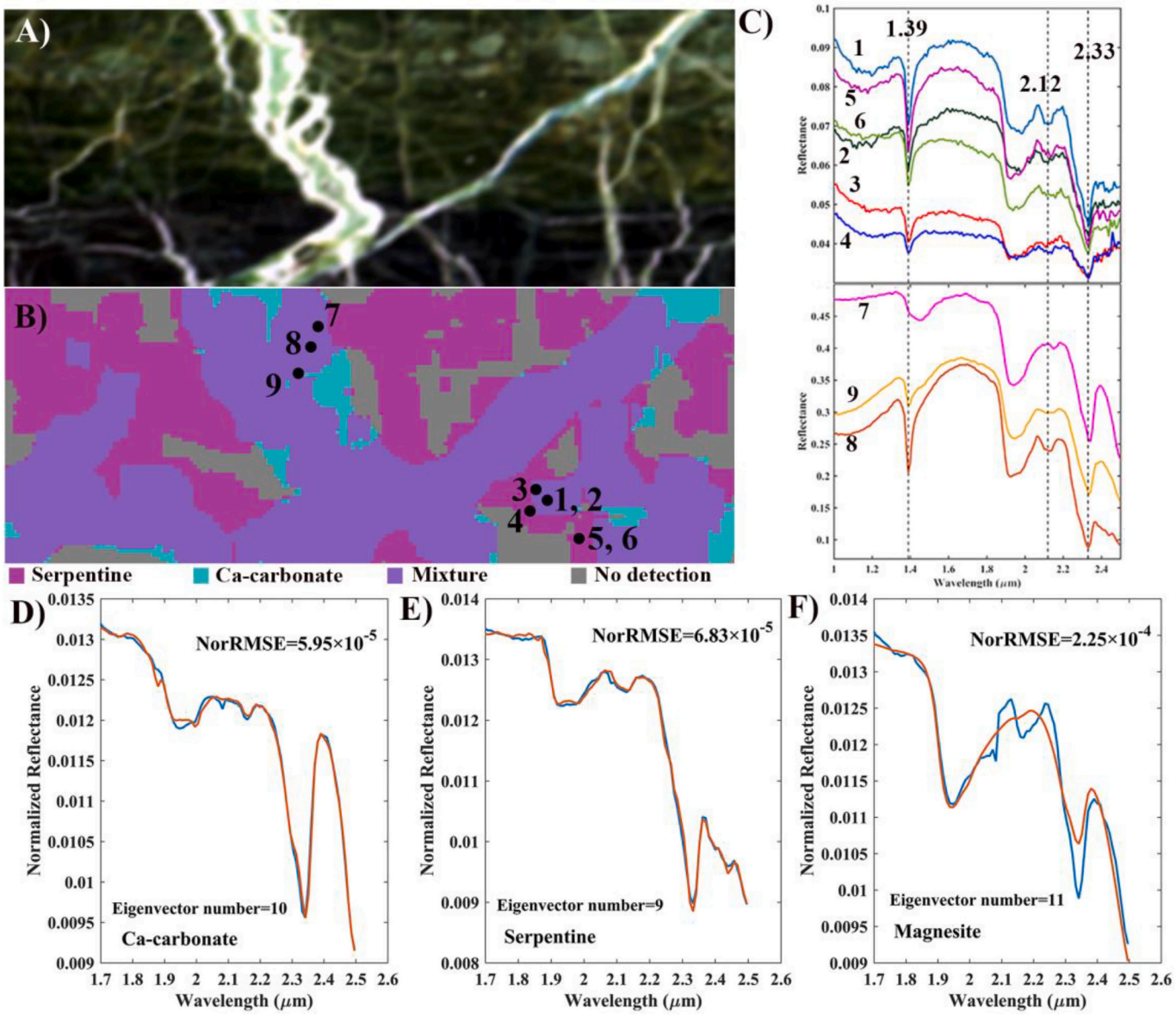

Fig. 4. VNIR spectra extracted from suggested detection locations generated via DAFA/TT analysis of a VNIR hyperspectral image of an Oman serpentinite hand sample. A) RGB composite of the VNIR hyperspectral data measured with a Headwall imaging spectrometer (R: 2.14 μm, G: 1.75 μm, B: 1.20 μm). B) The distribution of serpentine and Ca-carbonate. C) Example spectra extracted from the sites labeled in Fig. 4B. D) The FATT fit of all Ca-carbonate pixels to a calcite library spectrum. E). The FATT fit of all serpentine pixels to a serpentine library spectrum. F) The FATT fit to a magnesite library spectrum. The red spectrum is the library spectrum and the blue one is the modeled spectrum. (For interpretation of the references to colour in this figure legend, the reader is referred to the web version of this article.)

the calcium carbonate veins (Obeso and Kelemen, 2018).

3.1.2. Data acquisition

We used a Headwall imaging spectrometer (Headwall Photonics, Inc., Fitchburg, MA) with 9.62 nm spectral sampling interval, imaging at a spatial resolution of ~2.1 mm/pixel, and shortwave infrared (SWIR) wavelength range of 900–2600 nm to collect a hyperspectral image (Fig. 2B). Data near the edges of the sampled wavelength range (900–1000 nm, 2500–2600 nm) is of low signal-to-noise and is not used here. We collected a scan with an integration time of 10 ms per pixel row in a controlled laboratory setting to obtain data with high signal-noise ratio. We used a quartz halogen lamp as a light source. The data were converted from digital number to reflectance using a Spectralon© calibration panel. We also collected Raman spectra of the sample using a Horiba LabRAM HR confocal Raman spectrometer equipped with a 17 mW 633 nm HeNe laser, an astigmatic flat field spectrograph with focal length of 800 mm, and a multichannel air-cooled CCD detector.

3.2. CRISM data

CRISM data sampled from 365 to 3937 nm at a spectral resolution of 6.55 nm and with ~18–36 m/pixel spatial resolution were used in this study. CRISM images (FRT0000ABCB, FRT000093BE, FRT0000634B, HRL0000B8C2, and HRL000040FF) with previously reported magnesite or serpentine I/F detections were used to assess the performance of DAFA/TT (Ehlmann et al., 2009; Viviano-Beck et al., 2014). Another 45 CRISM images (Table S1) in different olivine-rich regions of Mars (Koeppen and Hamilton, 2008) were analyzed to detect serpentine outcrops, as serpentinization reactions typically occur in olivine-rich environments (Evans et al., 2013). All CRISM data were photometrically and atmospherically corrected with the CRISM Analysis Toolkit (CAT) (McGuire et al., 2009). We analyzed the wavelength region from

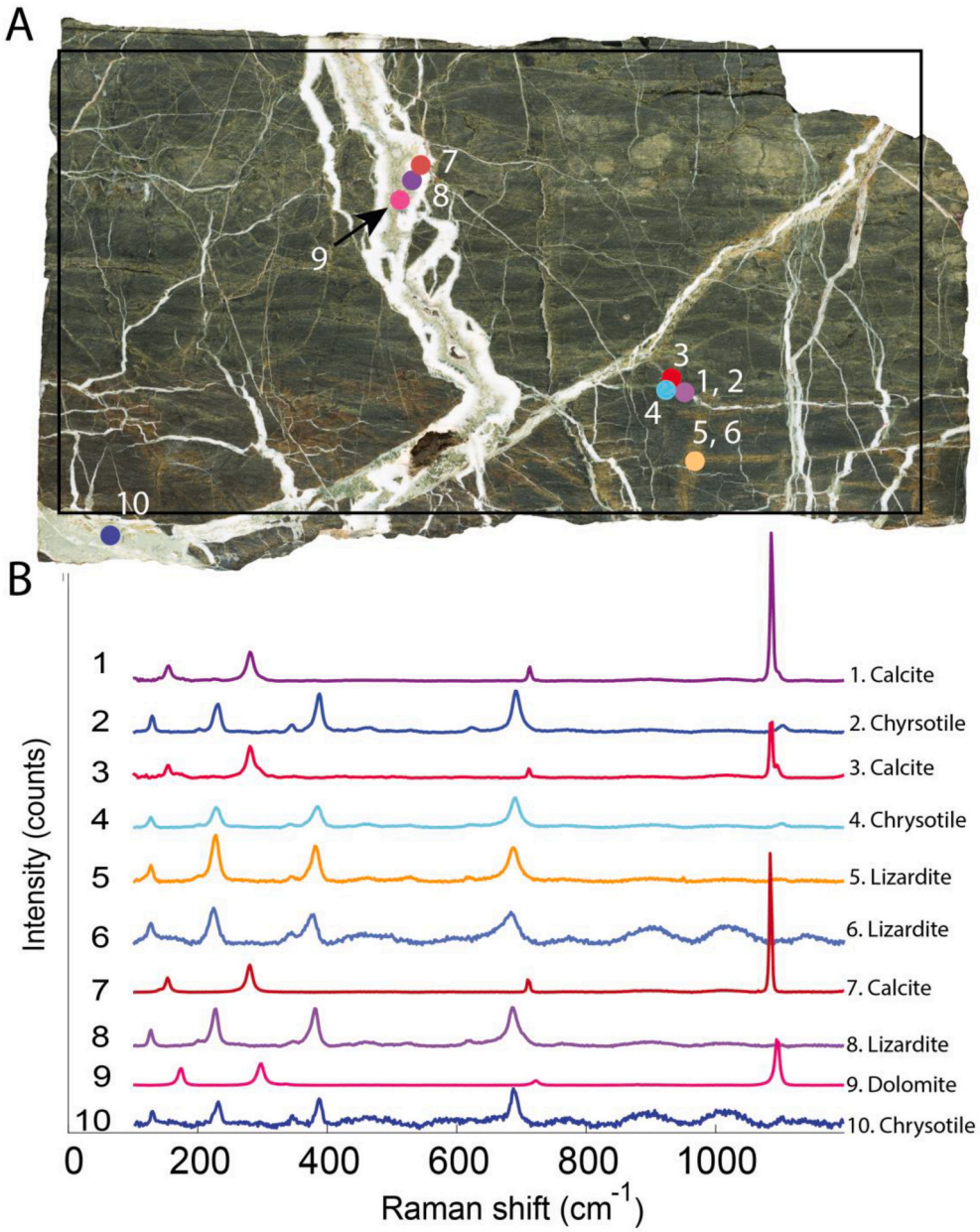

Fig. 5. (a) Scanned image of the Oman serpentinite hand sample with Raman spectra points labeled. The black box indicates the area covered in Figs. 2 and 4. There is a piece of serpentinite missing in the upper-right corner that broke off during cutting. (b) Raman spectra of locations labeled in a) and interpreted mineralogy.

1.7–2.6 μm because most diagnostic spectral features of aqueous minerals in CRISM data are located in this wavelength range subset (e.g., Clark et al., 1990; Thomas and Bandfield, 2017). To validate serpentine detections—which are all outcrops covered by relatively few pixels—we followed the methodology of Leask et al. (2018), where radiance data is atmospherically corrected, and ratioed to evaluate whether the presence of a detected 2.1 μm absorption can be attributed to serpentine rather than the 2.1 μm artifact present in CRISM TRR3 data.

3.3. Target spectra

Spectra of magnesite and Mg-rich serpentine (Fig. 3) were obtained from the Reflectance Experiment Laboratory (RELAB) spectral database and used in this study as targeted spectra to assess the performance of DAFA/TT. For this specific application of DAFA/TT, we used 54 serpentine and 77 carbonate library spectra (Table S2) to adequately represent the spectral variability of these phases on Earth.

4. Results

4.1. Application to laboratory hyperspectral data

DAFA/TT analysis of a Headwall hyperspectral image containing a serpentinite sample from the Oman ophiolite detected serpentine and Ca-carbonate, but no magnesite (Fig. 4), which is consistent with Raman spectral analysis of the sample (Fig. 5). Carbonate veins >1 mm thick were detected via DAFA/TT analysis of spectra collected with the Headwall imaging spectrometer, even at the subpixel scale (Fig. 5). Because the pixel size in this image is ~2 mm/pixel, and we detected Ca-carbonate veins ~1 mm in width, our analysis demonstrates that DAFA/TT is capable of suggesting detection of minerals at the half-pixel scale of Headwall hyperspectral images, but not at the quarter-pixel scale (Fig. 4). Spectra extracted from serpentine predicted locations (Fig. 4) show absorption features centered at ~1.39 μm, ~2.33 μm, and ~ 2.12 μm, which are consistent the presence of serpentine (e.g., Calvin and

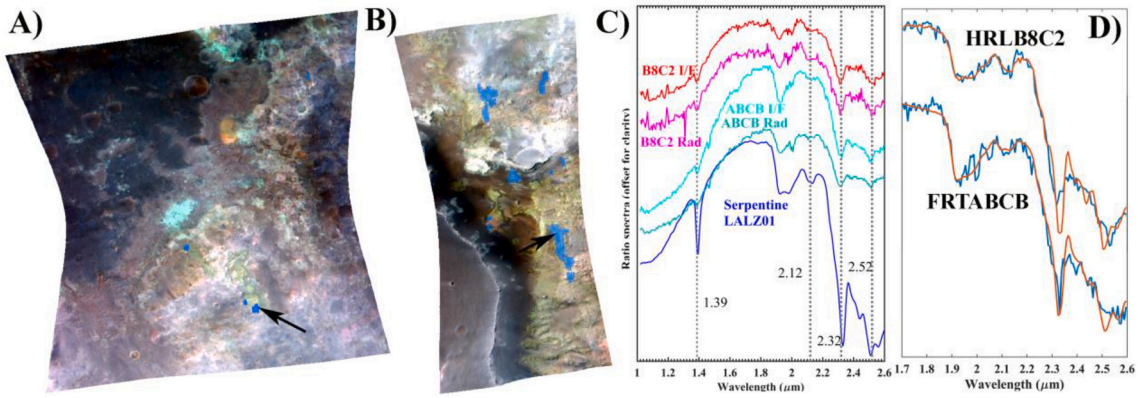

Fig. 6. Predicted serpentine locations from DAFA/TT analysis. A) The distribution of serpentine in FRT0000ABCB shown in blue. B) The distribution of serpentine in HRL0000B8C2 shown in blue. The background image is a CRISM colour composite (R: 2.38 μm, G: 1.80 μm, B: 1.15 μm). C) Previously identified serpentine spectra that correspond to regions indicated by the black arrows (Ehlmann et al., 2009). The locations from which these spectra were extracted were also verified by Leask et al. (2018) to not be CRISM TRR3 2.1 μm artifacts. D) The target transformation fits of all the serpentine clusters from DAFA/TT. The significant eigenvector number and NorRMSE for the DAFA/TT clusters in FRT0000ABCB are 9 and 1.12×10^{-4}, respectively. The significant eigenvector number and NorRMSE for the DAFA/TT clusters in HRL0000B8C2 are 23 and 1.16×10^{-4}, respectively. (For interpretation of the references to colour in this figure legend, the reader is referred to the web version of this article.)

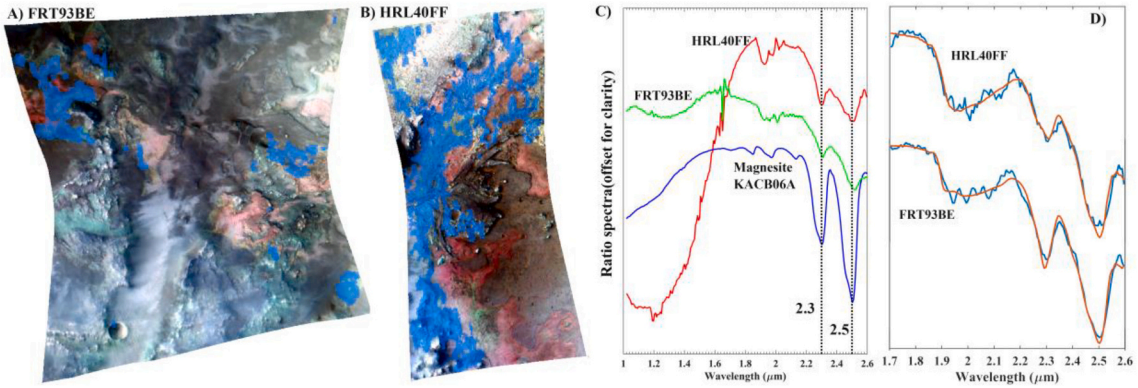

Fig. 7. Predicted magnesite locations from DAFA/TT. A) The distribution of magnesite in FRT000093BE shown in blue. B) The distribution of magnesite in HRL000040FF shown in blue. The background is a CRISM colour composite (R: 2.53 μm, G: 1.51 μm, B: 1.08 μm). C) The average spectrum of pixels from all DAFA/TT identified carbonate clusters in HRL000040FF and FRT000093BE, extracted with the ratio technique, compared to a magnesite library spectrum. D) The target transformation fits of all pixels predicted by DAFA/TT to have magnesite. The significant eigenvector number and NorRMSE for FRT000093BE are 12 and 6.04×10^{-5}, respectively. The significant eigenvector number and NorRMSE for HRL000040FF are 12 and 6.79×10^{-5}, respectively. (For interpretation of the references to colour in this figure legend, the reader is referred to the web version of this article.)

King, 1997; Bishop et al., 2008; Ehlmann et al., 2010). Spectra extracted from white veins (especially for points 7, 9 in Fig. 4B) contain 2.3 μm and 2.5 μm absorption features consistent with the presence of Ca-carbonate. Pixels containing mixed serpentine and Ca-carbonate were also identified (purple regions in Fig. 4B). Raman spectroscopic testing of mineral detections from VNIR hyperspectral image analysis demonstrated that DAFA/TT typically identifies the correct minerals within the sample, as well as their locations, down to the half-pixel scale. For DAFA/TT analysis using library spectra of other minerals (e.g. gypsum, kaolinite, talc), different hand-samples can be used to test DAFA/TT's performance in a laboratory setting. Serpentine with a shallow 2.12 μm absorption (e.g., spectrum 6 in Fig. 4C) was detected in the laboratory hyperspectral image using the DAFA/TT method. However, similar to how spectral mixing masks Ca-carbonate absorption features when Ca-carbonate subtends approximately less than half a pixel in Headwall imaging spectrometer data, spectral mixing at CRISM pixel spatial scales will weaken serpentine's diagnostic 2.12 μm absorption feature in the presence of other minerals. When the spectral signal from a given phase in a mixed system is too weak to impart variance on a given set of spectra, DAFA/TT cannot identify that phase within the mixed system.

4.2. Applications to CRISM data

4.2.1. Application to CRISM data containing previously reported mineral detections

CRISM image FRT000093BE (Fig. S5) was used to compare eigenvectors derived from previous factor analysis methods (Thomas and Bandfield, 2017) and the Hysime algorithm (Fig. S6-S7). The Hysime algorithm derived 11 eigenvectors, of which the first ~6 eigenvectors contain most of the useful spectral information. The other eigenvectors show significant noise, but they also contain some minor spectral information, which is important for reconstructing subtle diagnostic features (Thomas and Bandfield, 2017). Even though our eigenvector shapes are slightly different from previous factor analysis methods, the spectral features shown in the eigenvectors are largely similar. Thus, eigenvectors derived using the Hysime algorithm can be used to reconstruct endmember spectra. Modeled fits from the target library used in Thomas and Bandfield (2017) are shown in Fig. S8 and Fig. S9. The target transformation fit of magnesite, which was previously detected from FRT000093BE (Viviano-Beck et al., 2014), has a better fit quality when using Hysime derived eigenvectors (Fig. S10). More importantly, the number of signal subspace eigenvectors can be

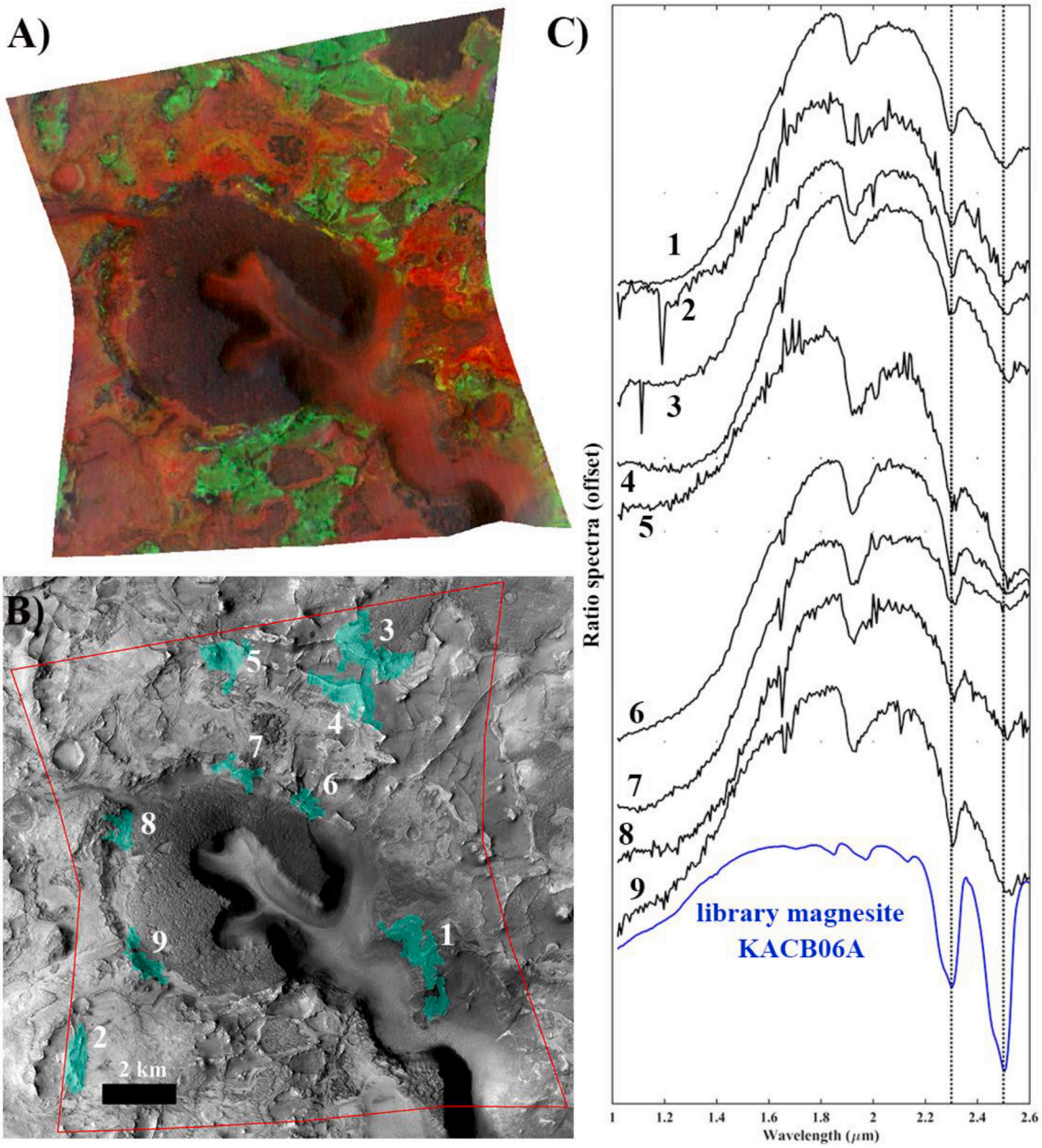

Fig. 8. DAFA/TT predicted locations of magnesite in FRT00003E12. A) CRISM spectral parameter map with R: OLINDEX, G: D2300, B: BD2500 overlain on CRISM RGB composite (R: 2.53 μm, G: 1.51 μm, B: 1.08 μm) (Lin et al., 2019). Red regions contain spectral features consistent with the presence of olivine, green regions contain spectral features consistent with the presence of phyllosilicate, and yellow regions contain spectral features consistent with the presence of carbonate-bearing rock (Ehlmann et al., 2008). B) DAFA/TT predicted locations of magnesite (turquoise regions). C) 3 × 3 pixel ratioed spectra from DAFA/TT clusters of magnesite in FRT00003E12. Target transformation fits of all DAFA/TT suggested detection clusters for magnesite are shown in the Fig. S9. (For interpretation of the references to colour in this figure legend, the reader is referred to the web version of this article.)

determined automatically.

Previously analyzed CRISM images (FRT000093BE, HRL0000B8C2, HRL000040FF, FRT0000634B and FRT0000ABCB) with well accepted, published I/F mineral detections were used to determine the optimal normalized RMSE threshold for DAFA/TT application to CRISM data for serpentine and magnesite detection. The normalized RMSEs of DAFA/TT fits from analysis of each CRISM observation are shown in Fig. S11. The normalized RMSEs for target transformation fits of magnesite are lower than those for serpentine, as magnesite is more widespread in these images. Clusters encompassing the previous mineral detections typically have normalized RMSEs lower than 1.50×10^{-4}. Thus, 1.5×10^{-4} is the normalized RMSE threshold for positive suggested detections during DAFA/TT analysis of CRISM images, meaning that serpentine and magnesite present in the images can be detected while minimizing false positives. DAFA/TT performs factor analysis and target transformation in differently shaped apertures of ~50 pixels, as opposed to the $\sim 10^5$ pixels in an entire CRISM image, therefore spatially localized serpentine or magnesite spectral features account for a greater fraction of spectral signal in the mixed system contained within an aperture. Thus, if serpentine or magnesite exist in the apertures, the normalized RMSE will typically be lower than 1.50×10^{-4}. The intersection of all the apertures yields the suggested distribution of serpentine and magnesite at the CRISM pixel scale. An optimal aperture size depends on data quality and signal strength. For obtaining high spatial accuracy and a sufficiently high signal-to-noise ratio, 50 pixels was selected as an empirical value for analysis of CRISM data. The aperture shapes are

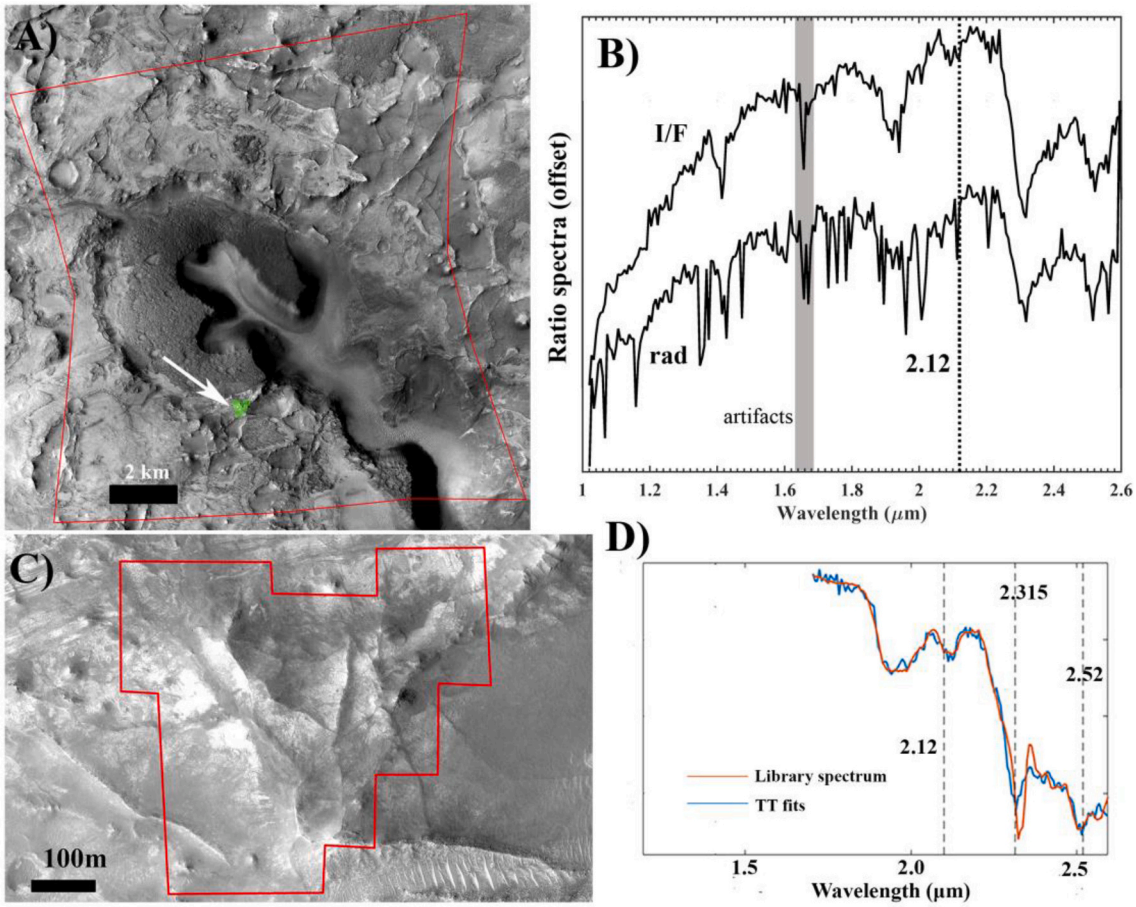

Fig. 9. A) DAFA/TT predicted location cluster for serpentine (green) in FRT00003E12, which was used to select pixels for extraction of a ratio spectrum (numerator: X: 368, Y: 72; denominator: X: 368, Y: 184; 3 × 3 average; unprojected FRT00003E12). The background is HIRISE image PSP_002888_2025. This suggested detection of serpentine was found to be the 2.1 μm artifact described by Leask et al. (2018) via extraction of a ratioed spectrum from radiance data converted to I/F. B) Ratioed spectra from within the DAFA/TT predicted location of serpentine. The ratioed TRR3 I/F data exhibits a 2.1 μm feature, while the ratioed radiance data converted to I/F does not, demonstrating that this 2.1 μm suggested detection is the TRR3 I/F artifact characterized by Leask et al. (2018). The greyed-out region near 1.7 μm corresponds to a particularly noisy region of CRISM spectra. C) Enlarged view of 2.1 μm artifact detection region in FRT00003E12, with the green cluster in (A) outlined in red. The background is HIRISE image PSP_002888_2025. D) The DAFA/TT modeled fit of the serpentine predicted location shown in A). The significant eigenvector number and NorRMSE are 26 and 1.36 × 10^{-4}, respectively. (For interpretation of the references to colour in this figure legend, the reader is referred to the web version of this article.)

illustrated in Fig. 1.

Results from DAFA/TT analysis of CRISM images with previously reported I/F detections of serpentine and magnesite is presented in Figs. 6 and 7. Fig. 6 shows predicted serpentine locations in FRT0000ABCB and HRL0000B8C2, which have good target transformation fits for serpentine (Fig. 6D). The general shape of the serpentine spectra can be fit well, the positions of the ~2.32 μm and ~2.52 μm features are slightly variable. This is likely caused by mixing of talc, saponite, carbonate, and serpentine, as occurs in spectra of natural serpentinite samples (Amador et al., 2017). Fig. 7 shows predicted magnesite locations from DAFA/TT in FRT000093BE and HRL000040FF. Predicted locations from DAFA/TT are consistent with previously reported identifications (Ehlmann et al., 2010; Goudge et al., 2015; Thomas and Bandfield, 2017) (Fig. 6C).

4.2.2. DAFA/TT predicted locations of serpentine and carbonate in CRISM data

In all the analyzed CRISM images, DAFA/TT suggested detections of magnesite are either associated with the regionally extensive Nili Fossae olivine-rich unit, the Jezero deltas, or the Jezero marginal carbonates, which agrees with previous work (Ehlmann et al., 2009; Goudge et al., 2015; Horgan et al., 2020). DAFA/TT suggested detections of magnesite in FRT00003E12 expand upon previous magnesite detections in this image (Ehlmann et al., 2008) and are supported via the extraction of ratioed spectra (Fig. 8). In FRT00003E12, we detected the same 2.1 μm artifact characterized by Leask et al. (2018), which is present in the majority of CRISM TRR3 images and can resemble the diagnostic 2.12 μm absorption of serpentine. Following Leask et al. (2018), we extracted ratioed spectra from TRR3 data as well as radiance data converted to units of I/F to differentiate 2.1 μm artifacts from true serpentine detections. In FRT00003E12, we detected 2.1 μm artifacts that are not true serpentine detections, as demonstrated by the generation of ratioed spectra from radiance data (Fig. 9). Most of these artifacts are present on ridge networks, which exhibit the albedo variations associated with the 2.1 μm artifact as described by Leask et al. (2018). After searching for serpentine in 44 other CRISM images (Table S1), we detected a small (27 pixel) serpentine outcrop in FRT00009971 that was validated via extraction of a ratioed spectrum from radiance data converted to I/F (Fig. 10). This adds to the 3 other validated serpentine detections on the surface of Mars from Leask et al. (2018).

5. Discussion

DAFA/TT is an effective method for highlighting the possible distribution of spectral signals, in this case from minerals, in hyperspectral images. It has already been applied to detect I/F spectra of small

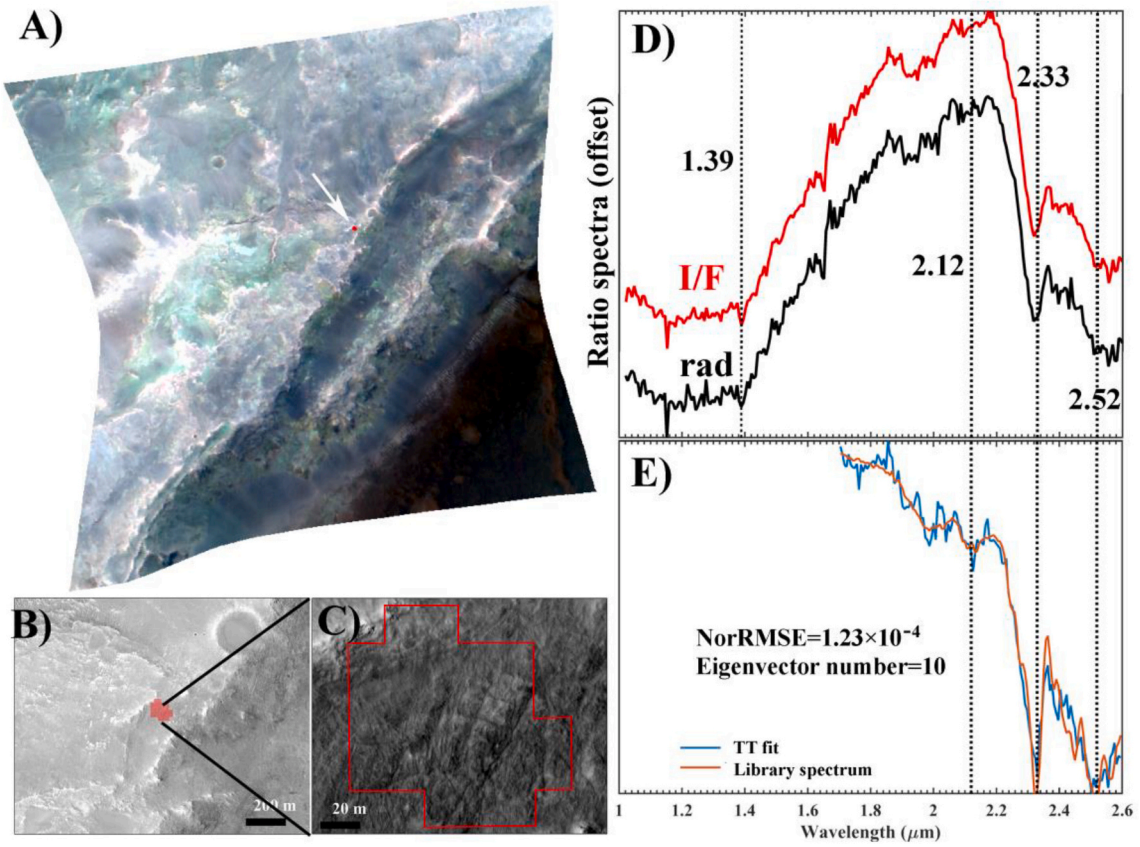

Fig. 10. Serpentine detection in Nili Fossae located using DAFA/TT. (A) Location of serpentine detection (red pixels) in FRT00009971. (B) Enlarged view of the serpentine detection (red pixels) in FRT00009971 overlain on HiRISE image PSP_006989_2025. (C) Most enlarged view of the serpentine detection in FRT00009971, outlined in red, on HiRISE image PSP_006989_2025. (D) Ratioed spectra from TRR3 I/F data (red) and radiance data converted to I/F (black). Both spectra exhibit features at 1.39 μm, 2.12 μm, 2.33 μm, and 2.52 μm that in combination are consistent with the presence of serpentine. (E) DAFA/TT fit to a serpentine library spectrum from the suggested detection cluster used to locate this serpentine outcrop in FRT00009971. (For interpretation of the references to colour in this figure legend, the reader is referred to the web version of this article.)

outcrops of hydrated silica and Al-phyllosilicate in Jezero crater and the Nili Fossae basement unit, as well as possible hydrated silica in the Nili Fossae olivine-rich unit (Tarnas et al., 2019). Though testing with laboratory data and CRISM data with previously characterized mineral detections indicated that DAFA/TT is robust to variations in signal-to-noise (Supporting information-text 1), caution must still be employed when interpreting its results. For example, DAFA/TT may pick up weak spectral signals from image-processing artifacts, such as the CRISM TRR3 artifact characterized by Leask et al. (2018) (Fig. 9). However, because information regarding the location of suggested detections is returned, artifacts and true serpentine detections can be differentiated by the same tests that Leask et al. (2018) applied to CRISM data. At this juncture, DAFA/TT suggested locations from modeled spectra should be supported with traditional I/F analysis to increase confidence in the veracity of detections. Still, for highlighting regions of interest within images and suggesting detections of weak, nearly hidden spectral signals in an automated fashion, DAFA/TT performs well relative to other techniques which are either time consuming (manual analysis) or do not characterize the spatial distribution of suggested locations for modeled spectra within a CRISM image (previous FATT applications) (Thomas and Bandfield, 2017; Amador et al., 2018). Because DAFA/TT generates predicted locations for weak spectral signals of minerals, validation tests, such as that required to verify serpentine detections on Mars (Leask et al., 2018), can be applied to potential detections.

Magnesite suggested detections made with DAFA/TT expand on previous detections within Nili Fossae (e.g., Ehlmann et al., 2008) and are associated with the regionally extensive olivine-rich unit, Jezero deltas, and Jezero marginal carbonates, agreeing with previous studies (Brown et al., 2010; Viviano et al., 2013; Goudge et al., 2015; Amador et al., 2017; Horgan et al., 2020; Brown et al., 2020). The detection of a 2.1 μm artifact in FRT00003E12, which was characterized in other CRISM TRR3 I/F images by Leask et al. (2018), was demonstrated by the extraction of ratioed spectra from both TRR3 I/F and radiance data converted to I/F. Serpentine in FRT00009971 is not associated with carbonate and it is not obvious which component of the Nili Fossae stratigraphy (Ehlmann and Mustard, 2012) this detection is associated with. This relatively small outcrop of serpentine, which was found after searching for serpentine in 45 CRISM images, adds to the 3 currently validated occurrences of serpentine on Mars (Leask et al., 2018) and demonstrates that DA/FATT can detect small outcrops of minerals on Mars with weak spectral signals. We found many 2.1 μm features in the 45 CRISM TRR3 images that ended up being artifacts (e.g., Fig. 9) relative to the number of 2.1 μm features that comprised true Mg-rich serpentine detections. This highlights the need to validate any claimed detection of serpentine on Mars using the radiance ratioed spectrum method of Leask et al. (2018). Any claimed detection that is incapable of doing this should not be considered to have both truly and confidently detected serpentine on Mars in CRISM data.

Even though the performance of DAFA/TT is good, there are some issues that need to be refined: 1) the accepted normalized RMSE needs to be determined more robustly and 2) some potential mineral locations cannot be predicted because of the lack of a fully comprehensive spectral library. Beyond serpentine and magnesite, other hydrated minerals like nontronite, saponite, talc, chlorite, illite, prehnite, and sulfate minerals will be evaluated with the DAFA/TT method in future work. DAFA/TT has already been used to detect I/F spectra of small outcrops of hydrated

silica and Al-phyllosilicate (Tarnas et al., 2019). We will characterize more outcrops with previously reported I/F mineral detections to constrain the proper fit quality threshold of target transformation for each specific mineral. The process of DAFA/TT is semi-automated, which makes it capable of analyzing large CRISM datasets. At this stage, we minimize false positive suggested detections by checking target transformation fits manually. It is possible that DAFA/TT could produce some false negative results, as is the case with any other hyperspectral analysis technique. At this juncture, DAFA/TT should be used to suggest the locations of minerals, then the presence of these minerals should be supported via generation of I/F spectra.

6. Conclusions

DAFA/TT is a new application of the FATT method. DAFA/TT is capable of mapping suggested locations of minerals from modeled spectra, in contrast to FATT which thus far has not been used to characterize the spatial distribution of minerals from modeled spectra. According to validations with laboratory and CRISM data, DAFA/TT accurately identified serpentine and magnesite at the CRISM pixel scale. The locations of magnesite in CRISM images FRT000093BE, HRL000040FF, and FRT00003E12 was predicted by DAFA/TT. These detections agree with and/or expand upon previous detections (e.g., Ehlmann et al., 2008; Goudge et al., 2015). Predicted locations for magnesite are associated with the regionally extensive olivine-rich unit, the Jezero deltaic unit, and the Jezero marginal carbonates unit, which is consistent with the results of previous studies (e.g., Ehlmann et al., 2008; Goudge et al., 2015; Viviano et al., 2013; Bramble et al., 2017; Amador et al., 2017; Horgan et al., 2020; Brown et al., 2020). DAFA/TT also detected the 2.1 μm artifact present in CRISM TRR3 I/F images as characterized by Leask et al. (2018), which was demonstrated by the extraction of ratioed spectra from 45 TRR3 I/F and radiance images that were converted to I/F. After searching through 45 images, we found a true detection of serpentine in FRT00009971, which was validated via extraction of ratioed spectra from TRR3 I/F and radiance data that were converted to I/F. This adds to the 3 other verified serpentine detections on Mars from Leask et al. (2018). The detection of many 2.1 μm artifacts relative to true serpentine detections also highlights the need for mineral detection techniques to specify the spatial location of suggested detections of minerals, otherwise validation methods such as those described by Leask et al. (2018) cannot be applied. Overall, DAFA/TT is useful for identifying potential outcrops of minerals with weak spectral signals, especially in large datasets. However, extraction of I/F spectra is necessary to verify DAFA/TT suggested detections and to avoid the reporting of false positive detections.

Declaration of Competing Interest

None.

Acknowledgments

We would like to thank and acknowledge Dr. Joshua Bandfield, the first individual to apply factor analysis and target transformation to data from Mars, for his insights and major contributions to this field. This work was supported by the National Natural Science Foundation of China (grant no. 41671360, 41525016, 41902318). JFM and JDT acknowledge NASA support through a subcontract from the Applied Physics Lab for CRISM investigations. H. Lin also acknowledges the support from the key research Program of the Institute of Geology and Geophysics, CAS (IGGCAS-201905). The Headwall imaging spectrometer was acquired using funds to JRK from The Institute at Brown for Environment and Society and Brown University. The DAFA/TT codes are available on GitHub (https://github.com/linhoml?tab=repositories).

Appendix A. Supplementary data

Supplementary data to this article can be found online at https://doi.org/10.1016/j.icarus.2020.114168.

References

Allen, D.E., Seyfried, W.E., 2003. Compositional controls on vent fluids from ultramafic-hosted hydrothermal systems at mid-ocean ridges: an experimental study at 400°C, 500 bars. Geochim. Cosmochim. Acta 67 (8), 1531–1542.
Amador, E.S., Bandfield, J.L., Brazelton, W.J., Kelley, D., 2017. The lost City hydrothermal field: a spectroscopic and astrobiological analogue for Nili fossae, Mars. Astrobiology. 17 (11), 1138–1160. https://doi.org/10.1089/ast.2016.1606.
Amador, E.S., Bandfield, J.L., Thomas, N.H., 2018. A search for minerals associated with serpentinization across Mars using CRISM spectral data. Icarus. 311, 113–134.
Bandfield, J.L., Christensen, P.R., Smith, M.D., 2000. Spectral data set factor analysis and end-member recovery: application to analysis of martian atmospheric particulates. J. Geophys. Res-Planet. 105 (E4), 9573–9587. https://doi.org/10.1029/1999je001094.
Bibring, J-P., Soufflot, A., Berthé, M., Langevin, Y., Gondet, B., Drossart, P., Bouyé, M., et al., 2004. OMEGA: Observatoire pour la Minéralogie, l'Eau, les Glaces et l'Activité. In Mars Express: the scientific payload 1240, 37–49.
Bioucas-Dias, J.M., Nascimento, J.M.P., 2008. Hyperspectral subspace identification. IEEE. T. Geosci. Remote. 46 (8), 2435–2445. https://doi.org/10.1109/Tgrs.2008.918089.
Bishop, J.L., Dyar, M.D., Sklute, E.C., Drief, A., 2008. Physical alteration of antigorite a Mossbauerspectroscopy, reflectance spectroscopy, and TEM study with applications to Mars. Clay Miner. 43, 55–67. https://doi.org/10.1180/claymin.2008.043.1.04.
Bramble, M.S., Mustard, J.F., Salvatore, M.R., 2017. The geological history of Northeast syrtis major, Mars. Icarus 293, 66–93. https://doi.org/10.1016/j.icarus.2017.03.030.
Brown, A.J., Hook, S.J., Baldridge, A.M., Crowley, J.K., Bridges, N.T., Thomson, B.J., Giles, M.M., Carlos, R., Bishop, J.L., 2010. Hydrothermal formation of clay-carbonate alteration assemblages in the nili fossae region of Mars. Earth Planet. Sci. Lett. 297 (1–2), 174–182.
Brown, A.J., Viviano, C.E., Goudge, T.A., 2020. Olivine-Carbonate Mineralogy of the jezero crater region. J. Geophys. Res-Planet. 125 (3), e2019JE006011 https://doi.org/10.1029/2019JE006011.
Bultel, B., Quantin, C., Lozac'h, L., 2015. Description of CoTCAT (complement to CRISM analysis toolkit). IEEE. J. Sel. Top. Appl. Earth. Obs. Remote. Sens. 8 (6), 3039–3049.
Calvin, W.M., King, T.V., 1997. Spectral characteristics of iron-bearing phyllosilicates: Comparison to Orgueil (CI1), Murchison and Murray (CM2). Meteorit. Planet. Sci. 32 (5), 693–701.
Carter, J., Poulet, F., Murchie, S., Bibring, J.P., 2013. Automated processing of planetary hyperspectral datasets for the extraction of weak mineral signatures and applications to CRISM observations of hydrated silicates on Mars. Planet. Space. Sci. 76, 53–67. https://doi.org/10.1016/j.pss.2012.11.007.
Chavagnac, V., Monnin, C., Ceuleneer, G., Boulart, C., Hoareau, G., 2013. Characterization of Hyperalkaline Fluids Produced by Low-Temperature Serpentinization of Mantle Peridotites in the Oman and Ligurian Ophiolites, G^3, 14, pp. 2496–2522.
Clark, R.N., King, T.V., Klejwa, M., Swayze, G.A., Vergo, N., 1990. High spectral resolution reflectance spectroscopy of minerals. J. Geophys. Res-Solid. 95 (B8), 12653–12680. https://doi.org/10.1029/JB095iB08p12653.
Clarke, A., Morris, G.J., Fonseca, F., Murry, B.J., Acton, E., Price, H.C., 2013. A low temperature limit for life on earth. PLoS One 8 (6), e66207.
Dundar, M., Ehlmann, B.L., Leask, E., 2019. Rare Phase Detections in Crism Data at Pixel-Scale by Machine Learning Generate New Discoveries about Geology at Mars Rover Landing Areas: Jezero and Ne Syrtis. LPI Contrib (No. 2132).
Edwards, C.S., Ehlmann, B.L., 2016. Carbon sequestration on Mars. Geology. 44 (6), E389. https://doi.org/10.1130/G37984y.1.
Ehlmann, B.L., Mustard, J.F., 2012. An in-situ record of major environmental transitions on early Mars at Northeast Syrtis Major. Geophys. Res. Lett. 39, 11202.
Ehlmann, B.L., Mustard, J.F., Murchie, S.L., Poulet, F., Bishop, J.L., Brown, A.J., Calvin, W.M., Clark, R.N., Des Marais, D.J., Milliken, R.E., Roach, L.H., 2008. Orbital identification of carbonate-bearing rocks on Mars. Science. 322, 1828–1832.
Ehlmann, B.L., Mustard, J.F., Swayze, G.A., Clark, R.N., Bishop, J.L., Poulet, F., Des Marais, D.J., Roach, L.H., Milliken, R.E., Wray, J.J., Barnouin-Jha, O., 2009. Identification of hydrated silicate minerals on Mars using MRO-CRISM: geologic context near Nili Fossae and implications for aqueous alteration. J. Geophys. Res-Planet 114. https://doi.org/10.1029/2009je003339.
Ehlmann, B.L., Mustard, J.F., Murchie, S.L., 2010. Geologic setting of serpentine deposits on Mars. Geophys. Res. Lett. 37 https://doi.org/10.1029/2010GL042596.
Evans, B.W., Hattori, K., Baronnet, A., 2013. Serpentinite: what, why, where? Elements. 9 (2), 99–106. https://doi.org/10.2113/gselements.9.2.99.
Gaffey, S., 1987. Spectral reflectance of carbonate minerals in the visible and near infrared (0.35–2.55 μm): anhydrous carbonate minerals. J. Geophys. Res-Solid. Earth. 92 (B2), 1429–1440. https://doi.org/10.1029/JB092iB02p01429.
Glotch, T.D., Bandfield, J.L., 2006. Determination and interpretation of surface and atmospheric miniature thermal emission spectrometer spectral endmembers at the meridiani planum landing site. J. Geophys. Res-Planet. 111 (E12), S06. https://doi.org/10.1029/2005JE002671.

Goudge, T.A., Mustard, J.F., Head, J.W., Fassett, C.I., Wiseman, S.M., 2015. Assessing the mineralogy of the watershed and fan deposits of the Jezero crater paleolake system, Mars. J. Geophys. Res: Planets. 120 (4), 775–808.
Goudge, T.A., Milliken, R.E., Head, J.W., Mustard, J.F., Fassett, C.I., 2017. Sedimentological evidence for a deltaic origin of the western fan deposit in Jezero crater, Mars and implications for future exploration. Earth. Planet. Sc. Lett. 458, 357–365. https://doi.org/10.1016/j.epsl.10.056.
Horgan, B., Anderson, R., Dromart, G., Amador, E., Rice, M., 2020. The mineral diversity of Jezero crater: evidence for possible lacustrine carbonates on Mars. Icarus. 339, 113526. https://doi.org/10.1016/j.icarus.2019.113526.
Hunt, G.R., Salisbury, J.W., 1971. Visible and near infrared spectra of minerals and rocks. II. carbonates. In: Modern Geology.
Kelley, D.S., Karson, J.A., Früh-Green, G.L., Yoerger, D.R., Shank, T.M., Butterfield, D.A., Hayes, J.M., Schrenk, M.O., Olson, E.J., Proskurowski, G., Jakuba, M., 2005. A serpentinite-hosted ecosystem: the lost City hydrothermal field. Science. 307, 1428–1434.
Keshava, N., Mustard J. F., 2002. Spectral unmixing. IEEE Signal Process. Mag. 19(1), 44-57. doi: https://doi.org/10.1109/79.974727.
Klein, F., Garrido, C.J., 2011. Thermodynamic constraints on mineral carbonation of serpentinized peridotite. Lithos 126 (3–4), 147–160.
Klein, F., Humphris, S.E., Guo, W., Schubotz, F., Schwarzenbach, E.M., Orsi, W.D., 2015. Fluid mixing and the deep biosphere of a fossil lost City-type hydrothermal system at the Iberia margin. PNAS 112, 12036–12041.
Koeppen, W.C., Hamilton, V.E., 2008. Global distribution, composition, and abundance of olivine on the surface of Mars from thermal infrared data. J. Geophys. Res: Planets. 113 (E5).
Leask, E.K., Ehlmann, B.L., Dundar, M.M., Murchie, S.L., Seelos, F.P., 2018. Challenges in the search for perchlorate and other hydrated minerals with 2.1-μm absorptions on Mars. Geophys. Res. Lett. 45 (22), 12–180.
Lin, H., Mustard, J.F., Zhang, X., 2019. A methodology for quantitative analysis of hydrated minerals on Mars with large endmember library using CRISM near-infrared data. Planet. Space. Sci. 165, 124–136.
Malinowski, E.R., 1991. Factor Analysis in Chemistry, 2nd ed. John Wiley, New York.
Malinowski, E.R., 1996. Automatic window factor analysis—a more efficient method for determining concentration profiles from evolutionary spectra. J. Chemom. 10, 273–279. https://doi.org/10.1002/(SICI)1099-128X(199607)10:4<273::AID-CEM418>3.0.CO;2-5.
Mayhew, L.E., Ellison, E.T., McCollom, T.M., Trainor, T.P., Templeton, A.S., 2013. Hydrogen generation from low-temperature water-rock reactions. Nat. Geosci. 6, 478–484.
McCollom, Klein T.M., F.,Robbins, M., Moskowitz, B., Berquo, T.S., Jons, N., Bach, W., Templeton, A., 2016. Temperature trends for reaction rates, hydrogen generation, and partitioning of iron during experimental serpentinization of olivine. Geochim. Cosmochim. Ac. 181, 175–200. https://doi.org/10.1016/j.gca.2016.03.002.
McCollom, T.M., Klein, F., Moskowitz, B., Berquó, T.S., Bach, W., Templeton, A.S., 2020. Hydrogen generation and Iron partitioning during experimental Serpentinization of an olivine–pyroxene mixture. Geochim. Cosmochim. Acta 282, 55–75.
McGuire, P.C., Bishop, J.L., Brown, A.J., Fraeman, A.A., Marzo, G.A., Morgan, M.F., Murchie, S.L., Mustard, J.F., Parente, M., Pelkey, S.M., Roush, T.L., 2009. An improvement to the volcano-scan algorithm for atmospheric correction of CRISM and OMEGA spectral data. Planet. Space. Sci. 57 (7), 809–815. https://doi.org/10.1016/j.pss.2009.03.007.
Miller, H.M., Mayhew, L.E., Ellison, E.T., Kelemen, P., Kubo, M., Templeton, A.S., 2017. Low temperature hydrogen production during experimental hydration of partially-serpentinized unite. GCA 209, 161–183.
Murchie, S., Arvidson, R., Bedini, P., Beisser, K., Bibring, J.P., Bishop, J., Boldt, J., Cavender, P., Choo, T., Clancy, R.T., Darlington, E.H., 2007. Compact reconnaissance Imaging Spectrometer for Mars (CRISM) on Mars Reconnaissance Orbiter (MRO). J. Geophys. Res-Planet. 112 (E5) https://doi.org/10.1029/2006je002682.
Mustard, J.F., Murchie, S.L., Pelkey, S.M., Ehlmann, B.L., Milliken, R.E., Grant, J.A., Bibring, J.P., Poulet, F., Bishop, J., Dobrea, E.N., Roach, L., 2008. Hydrated silicate minerals on Mars observed by the Mars reconnaissance orbiter CRISM instrument. Nature. 454 (7202), 305.
Mustard, J.F., Pieters, C.M., Isaacson, P.J., Head, J.W., Besse, S., Clark, R.N., Klima, R.L., Petro, N.E., Staid, M.I., Sunshine, J.M., Runyon, C.J., 2011. Compositional diversity and geologic insights of the Aristarchus crater from moon mineralogy mapper data. J. Geophys. Res: Planets. 116 (E6).
Obeso, J.C., Kelemen, P.B., 2018. Fluid rock interactions on residual mantle peridotites overlain by shallow oceanic limestones: insights from Wadi fins, sultanate of Oman. Chem. Geol. 498 (20), 139–149.
Parente, M., Saranathan, A.M., Wiseman, S., Ehlmann, B.L., Pan, L., 2014. Denoising CRISM images: a new look, in Proc. Lunar Planet. Inst. Sci. Conf. Abstr. 45, 2900. Mar.
Park, Ah-Hyung Alissa, Jadhav, Raja, Fan, Liang-Shih, 2003. CO2 mineral sequestration: chemically enhanced aqueous carbonation of serpentine. Can. J. Chem. Eng. 81, 885–890.
Pelkey, S.M., Mustard, J.F., Murchie, S., Clancy, R.T., Wolff, M., Smith, M., Milliken, R., Bibring, J.P., Gendrin, A., Poulet, F., Langevin, Y., 2007. CRISM multispectral summary products: parameterizing mineral diversity on Mars from reflectance. J. Geophys. Res-Planet. 112 (E8) https://doi.org/10.1029/2006je002831.
Rempfert, K.R., Miller, H.M., Bompard, N., Nothaft, D., Matter, J.M., Kelemen, P., Fierer, N., Templeton, A.S., 2017. Geological and geochemical controls on subsurface microbial life in the Samail ophiolite. Oman. Front. Micro. 8, 56.
Russell, M.J., Hall, A.J., Martin, W., 2010. Serpentinization as a source of energy at the origin of life. Geobiology. 8 (5), 355–371. https://doi.org/10.1111/j.1472-4669.2010.00249.x.
Schostack, K.J., Malinowski, E.R., 1993. Investigation of window factor analysis and matrix regression analysis in chromatography. Chemom. Intell. Lab. Syst. 20, 173–182. https://doi.org/10.1016/0169-7439(93)80013-8.
Schrenk, M.O., Brazelton, W.J., Lang, S.Q., 2013. Serpentinization, carbon, and deep life. Rev. Mineral. Geochem. 75 (1), 575–606. https://doi.org/10.2138/rmg.2013.75.18.
Schulte, Blake M., D., Hoehler, T., Mccollom, T., 2006. Serpentinization and its implications for life on the early Earth and Mars. Astrobiology. 6 (2), 364–376. https://doi.org/10.1089/ast.2006.6.364.
Seelos, F.P., Murchie, S.L., Humm, D.C., et al., 2011. CRISM data processing and analysis products updates-calibration, correction, and visualization. In: Lunar and Planetary Science Conference. 2011 Mar, p. 1438, 1608.
Sleep, N.H., Meibom, A., Fridriksson, T., Coleman, R.G., Bird, D.K., et al., 2004. H^2-rich fluids from serpentinization, geochemical and biotic implications. PNAS. 101, 12818–12823.
Smith, M.D., Bandfield, J.L., Christensen, P.R., 2000. Separation of atmospheric and surface spectral features in Mars global surveyor thermal emission spectrometer (TES) spectra. J. Geophys. Res-Planet. 105 (E4), 9589–9607. https://doi.org/10.1029/1999JE001105.
Takai, K., Nakamura, K., Toki, T., Tsunogai, U., Miyazaki, M., Miyazaki, J., Hirayama, H., Nakagawa, S., Nunoura, T., Horikoshi, K., 2008. Cell proliferation at 122 °C and isotopically heavy CH_4 production by a hyperthermophilic methanogen under high-pressure cultivation. PNAS 105, 10949–10954.
Tarnas, J.D., Mustard, J.F., Lin, H., Goudge, T.A., Amador, E.S., Bramble, M.S., Kremer, C.H., Zhang, X., Itoh, Y., Parente, M., 2019. Orbital identification of hydrated silica in Jezero crater, Mars. Geophys. Res. Lett. 46 (22), 12771–12782. https://doi.org/10.1029/2019GL085584.
Thollot, P., Mangold, N., Ansan, V., Le Mouélic, S., Milliken, R.E., Bishop, J.L., Weitz, C. M., Roach, L.H., Mustard, J.F., Murchie, S.L., et al., 2012. Most Mars minerals in a nutshell: various alteration phases formed in a single environment in Noctis Labyrinthus. J. Geophys. Res: Planets. 117 (E11).
Thomas, N.H., Bandfield, J.L., 2017. Identification and refinement of martian surface mineralogy using factor analysis and target transformation of near-infrared spectroscopic data. Icarus 291, 124–135. https://doi.org/10.1016/j.icarus.2017.03.001.
Vance, S.D., Hand, K.P., Pappalardo, R.T., 2016. Geophysical controls of chemical disequilibria in Europa. Geophys. Res. Lett. 43, 4871–4879. https://doi.org/10.1002/2016GL068547.
Viviano, C.E., Moersch, J.E., McSween, H.Y., 2013. Implications for early hydrothermal environments on Mars through the spectral evidence for carbonation and chloritization reactions in the Nili fossae region. J. Geophys. Res-Planet. 118 (9), 1858–1872. https://doi.org/10.1002/jgre.20141.
Viviano-Beck, C.E., Seelos, F.P., Murchie, S.L., Kahn, E.G., Seelos, K.D., Taylor, H.W., Taylor, K., Ehlmann, B.L., Wiseman, S.M., Mustard, J.F., Morgan, M.F., 2014. Revised CRISM spectral parameters and summary products based on the currently detected mineral diversity on Mars. J. Geophys. Res-Planet. 119 (6), 1403–1431. https://doi.org/10.1002/2014je004627.